

Design of a MEMS-based motion stage based on a lever mechanism for generating large displacements and forces

This content has been downloaded from IOPscience. Please scroll down to see the full text.

2016 J. Micromech. Microeng. 26 095008

(<http://iopscience.iop.org/0960-1317/26/9/095008>)

View [the table of contents for this issue](#), or go to the [journal homepage](#) for more

Download details:

IP Address: 129.6.33.137

This content was downloaded on 07/07/2016 at 01:06

Please note that [terms and conditions apply](#).

Design of a MEMS-based motion stage based on a lever mechanism for generating large displacements and forces

Yong-Sik Kim¹, Hongliang Shi², Nicholas G Dagalakis¹
and Satyandra K Gupta³

¹ Intelligent Systems Division, Engineering Laboratory, National Institute of Standards and Technology, 100 Bureau Dr., Gaithersburg, MD 20899, USA

² Former Research Associate in Intelligent Systems Division, Engineering Laboratory, National Institute of Standards and Technology, 100 Bureau Dr., Gaithersburg, MD 20899, USA

³ Department of Aerospace and Mechanical Engineering, University of Southern California, Los Angeles, CA, USA

E-mail: mk37do@gmail.com

Received 1 December 2015, revised 6 May 2016

Accepted for publication 14 June 2016

Published 6 July 2016



Abstract

Conventional miniaturized motion stages have a volume of 50–60 cm³ and a range of motion around 100 μm . Micro-electro-mechanical systems (MEMS)-based motion stages have been good alternatives in some applications for small footprint, micron-level accuracy, and a lower cost. However, existing MEMS-based motion stages are able to provide a force of μN level, small displacements (less than tens of microns), and need additional features for practical applications like a probe or a stage. In this paper, a single degree of freedom motion stage is designed and analyzed for a larger displacement, a larger output force, a smaller out-of-plane deformation, and a bigger moving stage for further applications. For these purposes, the presented motion stage is designed with a thermal actuator, folded springs, and a lever, and it is experimentally characterized. Furthermore, three different types of flexure joints are investigated to characterize their capabilities and suitability to serve as the revolute joint of the lever: a beam, a cartwheel, and a butterfly flexure. The presented motion stage has a moving stage of 15 mm \times 15 mm and shows a maximum displacement over 80 μm , and out-of-plane deformation under a weight of 120 μN less than 2 μm . The force generated by the actuator is estimated to be 68.6 mN.

Keywords: MEMS, motion stage, thermal actuator, folded beam

(Some figures may appear in colour only in the online journal)

1. Introduction

Micro-electro-mechanical system (MEMS)-based motion stages have been used in various application fields like metrology [1], cell manipulation [2, 3], micro-assembly [4], and optical scanning [5]. Their main advantages over conventional miniaturized motion stages [6, 7] are the resolution and accuracy of nanometer level and low costs resulting from the use of batch fabrication processes. The maximum range of motion for most MEMS-based motion stages is from

40 μm [6] to 50 μm [7] with sub-nanometer level resolution [8]. Their force generation also ranges from 11.7 μN [9] to 20 mN [6] depending on actuating mechanisms. With these capacities, the largest dimensions of the motion stages range from 350 μm [10] to 3 mm [11].

A conventional miniaturized motion stage widely used in precision motions is able to generate a motion displacement larger than 100 μm and also produce a force up to 10 N. In order to achieve these capabilities, the moving stage needs to

be designed large. The XYZ Piezo Stage⁴ [12] has a moving stage of 44 mm × 44 mm, which can be used as a testbed for a test sample. Compared with the miniaturized motion stages, MEMS-based motion stages have their advantages in their small footprint and cost, but they provide a shorter stroke and a limited force, and are also fragile. In addition, most MEMS-based motion stages lack a moving stage, therefore it is not easy to interact with an object or position a sample without additional features like micro-manipulators.

In order to extend the application of MEMS-based motion stages, it is necessary to improve the capabilities that are currently inferior to conventional miniaturized motion stages. Examples of those include the range of motion, force, stiffness, and a manipulating moving stage. To illustrate the design requirement, the required specifications for rheological applications are selected as a reference. Rheometers are designed to measure the flow properties of viscoelastic materials [13] trapped between two parallel plates [14, 15]. These two plates consist of an actuating plate and a stationary plate. When a sample material is placed between the two plates, the actuating plate applies a shear strain to the sample and its response is measured to calculate its viscoelastic properties. In this application, a MEMS-based motion stage can be a good alternative to replace the actuating plate [13]. Many rheological measurements were done with the operating frequency between 0.2 Hz [16] and 1 Hz [17], and the shear or storage modulus from 100 Pa to 1.3 MPa [17]. In addition to these design parameters, a large moving stage is also needed to be able to apply the well-distributed shear force to a test sample. The gap between the parallel plates must be larger than any grain size of a test material, which is roughly 80 μm for a cementitious material [18].

For these reasons, an actuator and a displacement amplifying mechanism are designed and analyzed. The commonly used actuating mechanisms in MEMS are electrostatic [19–21], magnetic [4, 22, 23] and thermal [24, 25]. Magnetic and electrostatic actuators are well known for their stable response at high frequency range, but their μN level force makes it difficult to provide an adequate force in some applications. Thermal actuators are able to generate mN level force [25, 26], however they generate a short range of motion. In order to overcome the small stroke, a displacement amplifier is adopted in MEMS applications such as a compliant displacement amplifier [11] and a lever mechanism [7, 27]. The compliant displacement amplifier, consisting of two long slender beams and one pivoted beam, is able to amplify up to more than 3.17 times with a force less than 3 mN [11]. However, this amplifier requires a relatively larger area than a lever mechanism and it is not easy to analyze the analytic model depending on applications. Contrary to this, the lever mechanism is well analyzed in conventional designs, so it is possible to adjust the amplifying ratio reasonably. In addition to this, its footprint is smaller than that of the compliant displacement amplifier, so it is easier to embed a lever into the existing devices without a significant design modification.

⁴Certain commercial equipment is identified in this paper to adequately describe the experimental procedure. Such identification does not imply recommendation or endorsement by the National Institute of Standards and Technology nor does it imply that the equipment identified is necessarily the best available for the purpose.

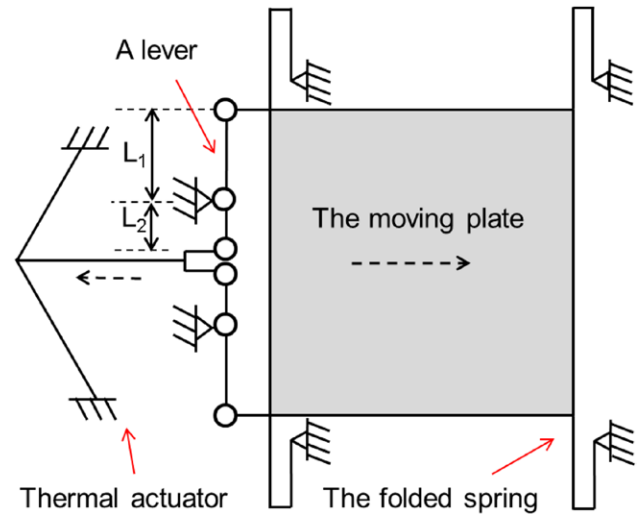


Figure 1. The schematic diagram of the presented one DOF motion stage.

In this paper, a MEMS-based motion stage is presented for providing a displacement larger than the existing motion stages, a mN level force, sufficient stiffness to prevent out-of-plane deformation, and a large moving stage. The design and the analysis processes are presented for this stage, which is composed of a thermal actuator, a lever mechanism, a moving stage, and the four folded springs. The lever mechanism is implemented with three different types of flexures. The comparison of those flexures is proposed to evaluate their performance. The presented motion stage is fabricated and experimentally tested for its maximum displacement and out-of-plane deformation with additional weight on its moving stage.

2. Mechanical design

The presented in-plane single degree of freedom (DOF) motion stage is composed of an actuator, a moving stage, and two levers. Its schematic diagram is shown in figure 1, where the solid lines stand for the beams and the circles represent mechanical hinges allowing rotational motions through their elastic deformations. The moving stage is 3.2 mm × 2.7 mm in size and is supported by four folded springs, which are designed to be flexible for its designated 1-DOF translational motion while being stiff against other directions. A lever mechanism consisting of two levers connects the actuator and the moving stage, and converts some portion of force into a large displacement. Based on this combination, the displacement of the moving stage, U_{plat} can be expressed as a function of the design parameters of the actuator and the lever [7] as:

$$U_{\text{plat}} = \left(\frac{L_1}{L_2} \right) \frac{F_{\text{act}}}{K_{\text{act}} + \left(\frac{L_1}{L_2} \right)^2 K_{\text{plat}}} \Delta T_{\text{ave}}, \quad (1)$$

where, F , K , and U represent force, stiffness, and displacement. The subscript act and plat represent the actuator and the moving stage, respectively. ΔT_{ave} is the average temperature rise in the actuator. Each parameter shown in equation (1) is optimized to maximize the displacement and force in the following sections.

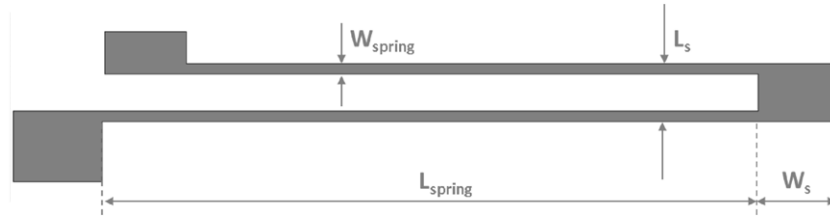


Figure 2. The folded spring design.

For practical applications, the design requirements are defined broadly: (1) the total size is less than 10 mm × 10 mm.; (2) the beam thickness (T) of the actuator is 30 μm , which is pre-determined by the thickness of the silicon on insulator (SOI) wafers used in the fabrication; (3) all other beam dimensions should be larger than 10% of the beam thickness (T). This is because the Bosch⁴ deep reactive ion etching (DRIE) process [28] recommends a high-aspect ratio less than 1:10 for reliable etching operations.

2.1. The folded spring design of the moving stage

The folded spring used to suspend the moving stage is shown in figure 2. It consists of two long slender beams and one short pivoted beam. It is designed to be flexible for a designated in-plane motion and stiff against movement in any other direction. The folded spring determines the whole stiffness of the moving stage and also affects the design of the lever. The stiffness of the motion platform, K_{spring} can be expressed [29] as:

$$K_{\text{spring}} = \frac{mET}{\left(\frac{L_{\text{spring}}^3}{2W_{\text{spring}}^3} + \frac{6(1+\mu)L_{\text{spring}}}{5W_{\text{spring}}} + \frac{L_s}{2W_s} + \frac{3L_{\text{spring}}^2L_s}{2W_s^3} \right)} \quad (2)$$

where μ is the Poisson's ratio of silicon. Other design parameters are illustrated in figure 2. Parameter values are listed in table 1. Based on equation (2), the stiffness of the motion platform is calculated to be 53.4 N m⁻¹, while a finite element analysis (FEA) model gives a stiffness of 51.76 N m⁻¹ indicating that the analytical model is very accurate with an error of only 3.17%.

2.2. The thermal actuator design

The actuator used in the presented motion stage is a bent-beam type or a chevron-type thermal actuator [30]. This actuator looks like a chevron and utilizes the thermal expansion of beams to produce a motion along its shaft. The main design parameters, except for the beam thickness (T), are illustrated in figure 3. The analytic relationship of the stiffness and the force of the bent-beam type electrothermal actuator are derived from previous studies [31]. Based on the analytical model [27] and the existing designs [7], the initial values are selected for each design parameter for the optimization process.

One thing to notice is the beam width (W). The bent beams in the actuator can be regarded as a slender axial-load carrier [31]. When the force generated by the actuator is larger than the critical buckling load of the beam, the beam starts buckling [7]. In this case, the maximum displacement or force from a thermal actuator can be limited by the buckling of beams [32].

Table 1. The design parameters.

Symbol	Component	Design parameter	Values
W	Actuator	Beam width	27 μm
θ		Beam angle	2°
L	Lever	Beam length	1520 μm
T		Beam thickness	30 μm
n	Lever	Number of beams	10
L_1		Long lever length	1160 μm
L_2		Short lever length	180 μm
t	Compliant joint	Beam width	7 μm
b		Beam length	150 μm
m	Folded spring	Number of the folded springs	4
W_s		Short beam width	155 μm
L_s		Short beam length	100 μm
W_{spring}		Long beam width	20 μm
L_{spring}		Long beam length	1000 μm
L_{plat}	Moving stage	Length	3200 μm
W_{plat}		Width	2700 μm

In addition, any out-of-plane buckling also should be avoided by making the beam width (W) narrower than the beam thickness (T) [7]. These relationships can be summarized as:

$$\sqrt{\frac{12\alpha\Delta T_{\text{ave}}}{n\pi^2}} L < W < T \quad (3)$$

where α is the coefficient of thermal expansion of silicon. The beam width (W) is limited based on equation (3) to avoid any unwanted buckling or deformation.

An additional design constraint is a thermal melting-down condition, because the thermal actuator is made of silicon and is limited by the material properties of silicon; the temperature over its maximum endurable limit causes serious structural damage or permanent deformation. For this reason, the temperature rise in a thermal actuator should be limited to 550 °C [24] for a reliable operation.

In order to evaluate the important design parameters quantitatively and get the optimization trend, the sensitivity analysis is applied to the actuator design [33]. This analysis monitors the output by varying one design parameter, and measures its effect. This sensitivity analysis is implemented by utilizing the NIST 10-step analysis software [34, 35], which is based on the 2^k factorial design ([36], 218–9) and results from finite element analysis (FEA) ([36], 170–1). In this analysis, the ranges of four main design parameters are determined; the beam length (L) between 800 and 1200 μm , the beam width (W) between 12 and 16 μm , the beam angle (θ)

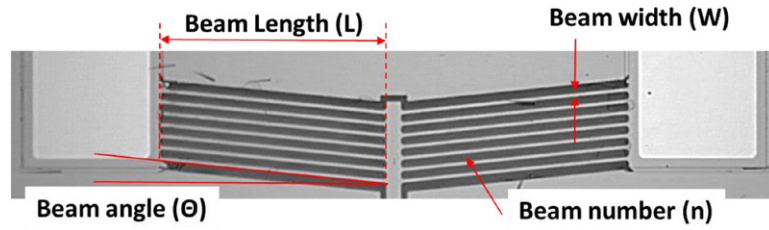


Figure 3. The adopted thermal actuator for the motion stage.

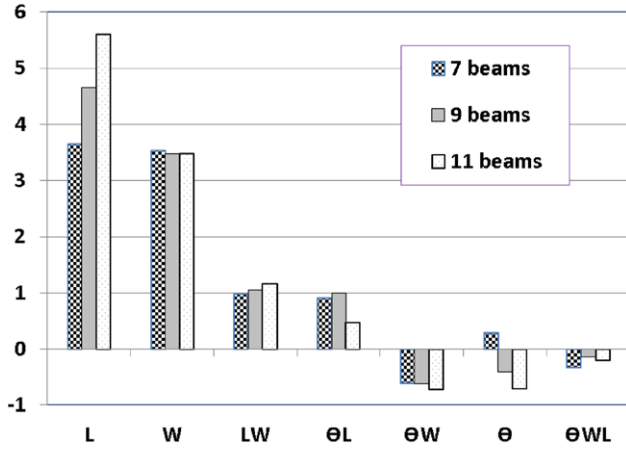


Figure 4. The effect of each design parameter of the thermal actuator based on the sensitivity analysis.

between 3 and 5°, and the beam numbers (n) with 7, 9, and 11. The linear relationship between the output and the design parameters with eleven beams is obtained and expressed as:

$$U_{\text{plat}} = 5.60L + 3.48W + 1.16LW - 0.71\theta W - 0.71\theta + 0.48\theta L - 0.20\theta LW. \quad (4)$$

With different beam numbers, all parameters are numerically evaluated with their initial values and summarized in figure 4: (1) the beam length (L) is more dominant than the others; (2) the beam width (W) is also an important factor; (3) the longer beam length (L) is desirable with higher beam numbers (n); and (4) the third important factor is the interaction between the beam length (L) and the beam width (W).

Based on these observations, the new parameters for the beam length (L), the beam width (W), and the beam number (n) are determined and the same analysis repeats itself to find the close values for their optimum within the allowable area. The beam length and the beam width tend to be larger under the given area, but the beam angle has its own optimum value between 2 and 5°. Based on the determined design parameters, a total of 41 models are created and their FEA results are compared with each other to find the optimum value with the given design parameters.

2.3. The lever ratio

The lever used in the presented motion stage plays an important role in balancing between the force and the displacement of the moving stage. Since the force from MEMS actuators is generally not high enough, we need to analyze the lever mechanism to find the optimum lever ratio with the given

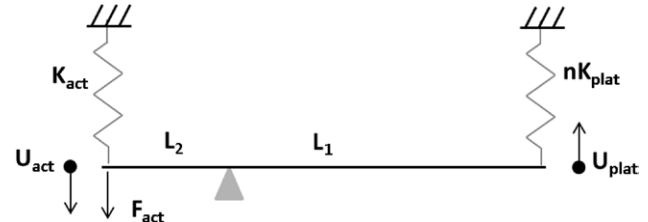


Figure 5. The lever mechanism in the presented motion stage.

design. For this analysis, the lever used in the motion stage is described in figure 5, where the right side is connected to the moving stage, the middle flexure hinge works as a pivot, and the left side is linked to the actuator. Based on this schematic diagram, the conservation of the moment can be expressed as:

$$F_{\text{act}}V_{\text{act}} = F_{\text{plat}}V_{\text{plat}} \quad (5)$$

where V_{act} and V_{plat} are the velocities of the actuator and the moving stage, respectively. Equation (5) can be further written as:

$$F_{\text{act}} \frac{dU_{\text{act}}}{dt} = F_{\text{plat}} \frac{dU_{\text{plat}}}{dt} \quad (6)$$

These two displacements are tightly linked by the lever, so their relationship can be expressed as:

$$\left(\frac{L_1}{L_2}\right)dU_{\text{act}} = dU_{\text{plat}} \quad (7)$$

where, L_1 and L_2 are the lengths of the two segments of the lever, as shown in figures 1 and 5. With equations (6) and (7), the stiffness of the actuator can be rewritten as:

$$K_{\text{act}} = \frac{F_{\text{act}}}{dU_{\text{act}}} = \frac{\left(\frac{L_1}{L_2}\right)F_{\text{plat}}}{dU_{\text{act}}} = \frac{\left(\frac{L_1}{L_2}\right)F_{\text{plat}}}{\frac{dx_{\text{plat}}}{\left(\frac{L_1}{L_2}\right)}} = \left(\frac{L_1}{L_2}\right)^2 \frac{F_{\text{plat}}}{dU_{\text{plat}}} = \left(\frac{L_1}{L_2}\right)^2 K_{\text{plat}} \quad (8)$$

where, K_{plat} is the stiffness of the whole moving stage, which comes from both the rotational joints and the K_{spring} . Equation (8) indicates that the stiffness is proportional to the square of the lever ratio. Based on equation (8) and the free-body diagram in figure 5, the displacement of the moving stage can be expressed [7] as:

$$U_{\text{plat}} = \left(\frac{L_1}{L_2}\right)U_{\text{act}} = \left(\frac{L_1}{L_2}\right) \frac{nF_{\text{act}}}{K_{\text{act}} + \left(\frac{L_1}{L_2}\right)^2 K_{\text{plat}}} \quad (9)$$

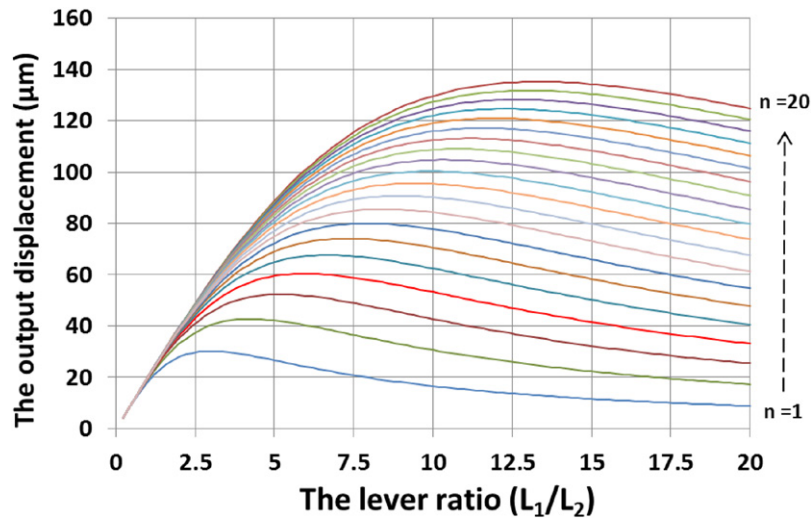


Figure 6. The expected maximum displacement with different lever ratios and beam number (n).

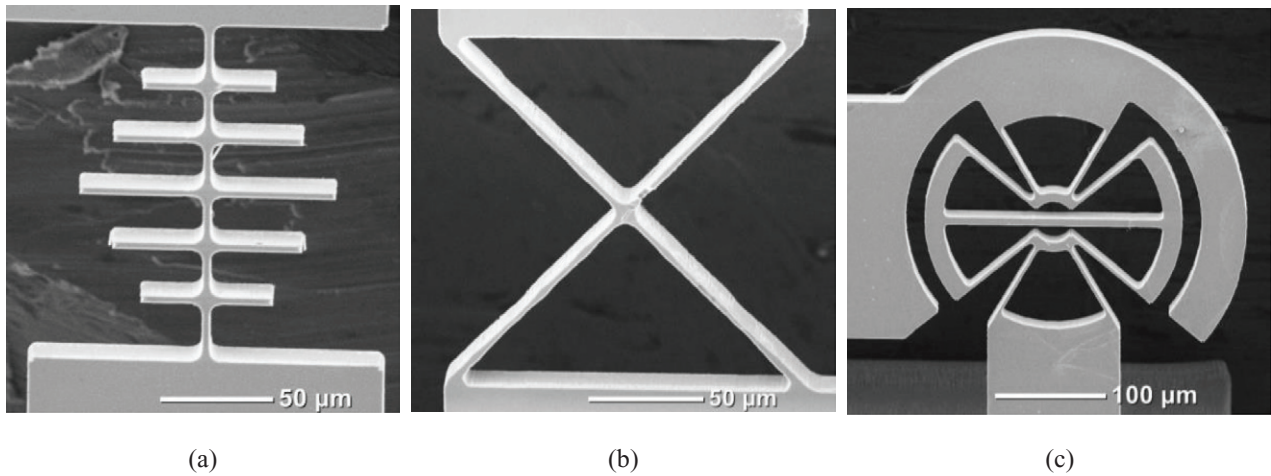


Figure 7. Three types of flexure hinges. (a) Beam type. (b) Cartwheel type. (c) Butterfly type.

Based on equation (9), the output displacements are calculated and plotted in figure 6, as a function of the lever ratio and the beam number (n). In figure 6, the output displacement is linearly proportional to a lever ratio less than 1:3, which means that the actuator provides enough force for the lever with a small amplifying ratio. This linear increment starts decreasing gradually with a lever ratio larger than 1:3 and then reaches its own optimum point around 1:7–12 depending on beam number. After this global maximum point, the displacement starts decreasing slowly. This characteristic comes from the fact that the force from the actuator is not sufficiently large to move the moving stage through a lever mechanism. From this analysis, twelve beams and the lever ratio of 1:9 are selected to utilize all available area in the given footprint.

2.4. Three lever flexure joints candidates

Three different types of flexure hinge designs are applied to the lever and compared with each other to evaluate their performances. The three types of flexure hinges are shown in

figure 7. Figure 7(a) is a typical beam with five ribs which facilitate the accurate etching of this long flexure during the MEMS fabrication, since a long slender beam tends to be thinner and break during its fabrication. Figure 7(b) is a cartwheel type design or a combination of two beams, which has been used in precision motion stages [37] and is relatively stiffer than the single beam type. Figure 7(c) is a butterfly type [38], well known for a pure rotational motion.

The maximum translational displacement of the moving stage is limited by the maximum rotational angles of the used flexures. Based on the geometric relationship in figure 1, the maximum displacement of the moving stage, ΔU_{\max} can be described as a function of the lever length, L_1 as:

$$\Delta U_{\max} = \theta_{\max} \cdot L_1 \tag{10}$$

where θ_{\max} is the maximum rotational angle. The maximum rotational angle will happen when the stress on the flexure is close to the yield strength of silicon (5–9 GPa [39]). Based on this relationship, the three types of flexures are applied to the levers as shown in figure 8, which are experimentally tested and compared with each other.

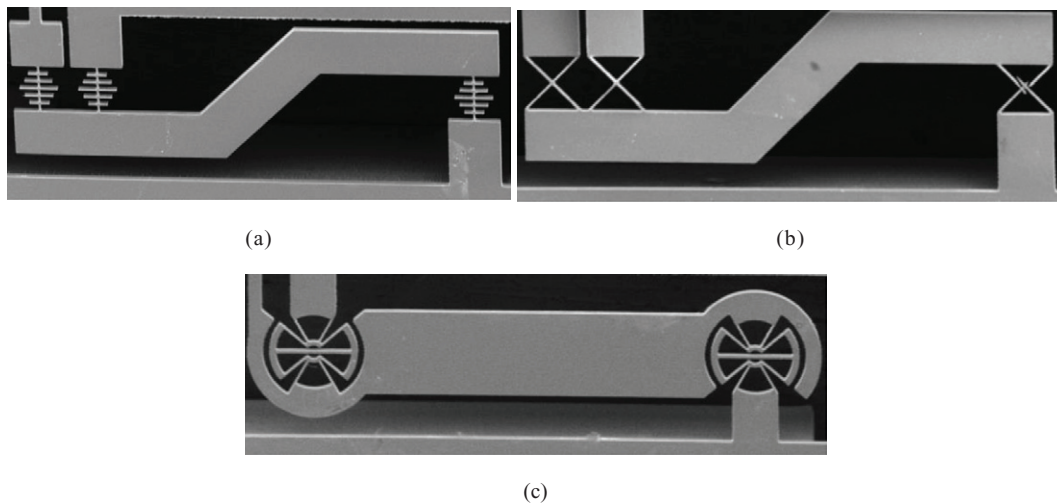


Figure 8. The lever with three types of flexures. (a) The beam flexures. (b) The cartwheel flexures. (c) The butterfly flexures.

3. Finite element analysis (FEA)

Finite element analysis (FEA) using ANSYS⁴ is utilized to analyze the behavior of the motion stage and the three types of flexures. For accurate analysis, the assumptions for structural and thermal boundary conditions are applied as follows: (1) the only electrical connection is to the actuator; (2) all the ends of the folded springs, the pivots, and both ends of the actuator are firmly fixed to a ground and connected to a heat sink with a room temperature of 20 °C. The material properties used in the FEA are: Young's modulus of 130 GPa, resistivity of 0.01 Ωcm, and yield strength of 7 GPa.

The maximum force that the actuator needs to generate is numerically calculated, because this force is directly related to the shear stress. The shear stress mentioned in the introduction ranges from 100 Pa to 1.3 MPa, indicating that the presented actuator is required to apply a force level from 9.86 mN–11.2 mN to the moving stage. The thermal actuator with a single beam is able to generate a force of 6.86 mN. This value is in the target range and can increase by incorporating more beams. The maximum force of a thermal actuator with ten beams will be about 68.6 mN.

The stiffness of the actuator and the moving stage is also numerically investigated in this FEA. The stiffness of the actuator, K_{act} is expected to be 115.29 N m⁻¹ based on the FEA. The stiffness of the actuator also increases proportional to the beam number (n) and will be 1152.9 N m⁻¹ with ten beams. With four folded springs, the stiffness of the moving stage, K_{stage} is 46.28 N m⁻¹ based on the FEA.

The frequency response of the motion stage with beam flexure is also analyzed with a harmonic forced response test by applying a cyclic load at the thermal actuator. The 1st resonance frequency of the design of the presented motion stage with the beam flexure or the cartwheel flexure is expected to be around 2 kHz or higher. The structure of the presented motion stages is stable for the operations up to that ranges of frequencies. However, 1st resonance frequency of the thermal actuator itself is less than 0.7 kHz [7], due to its heating and cooling time. Thus, it is desirable to utilize the presented

motion stage with frequencies less than 100 Hz for stable operations.

4. Micro-fabrication

The whole fabrication process of the motion stage is based on the silicon-on-insulator multi-user multi-processes (SOIMUMPs) [40]. A silicon-on-insulator (SOI) wafer is used as a starting material with a 30 μm thick device layer for the main device structures, a 400 μm thick handle layer for the backside frame, and a 2 μm thick buried oxide layer between them. The first step in the fabrication process is the deposition of the pad metal consisting of a first top layer of 50 nm chrome and a second layer of 500 nm gold for the electric connection of the thermal actuator to an external power supply. The following step is to transfer the main designs on the device layer with deep reactive ion etching (DRIE). The buried oxide layer in the middle of an SOI wafer works as an etching stop layer for this DRIE. After finishing the fabrication on the device layer of the SOI wafer, the handle layer of the SOI wafer is also processed with the same method used for the device layer to release the main components on the device layer. After the two DRIE steps, the remaining oxide layer is eliminated and the motion stage on the wafer is free to move. After packing and wire-bonding, the fabricated motion stage is ready to operate.

The motion stage fabricated using the micro-fabrication process is shown in figure 10(a), where the scanning electron microscope (SEM) image clearly shows an actuator (top), four folded springs (left and right), two levers, and a moving stage (middle). The moving stage has additional features like circular patterns made of metal or the device layer to increase its contact area with the target materials. The footprint of the moving stage is 3.2 mm × 2.7 mm and can contain more than a few nano-liters of fluid volume. The detailed image of the folded spring is shown in figure 10(b). Figure 10(c) shows the connecting mechanism between the actuator and the lever. In order to electrically isolate the moving stage, the connecting shaft has a deep isolating trench, but its trench backside is

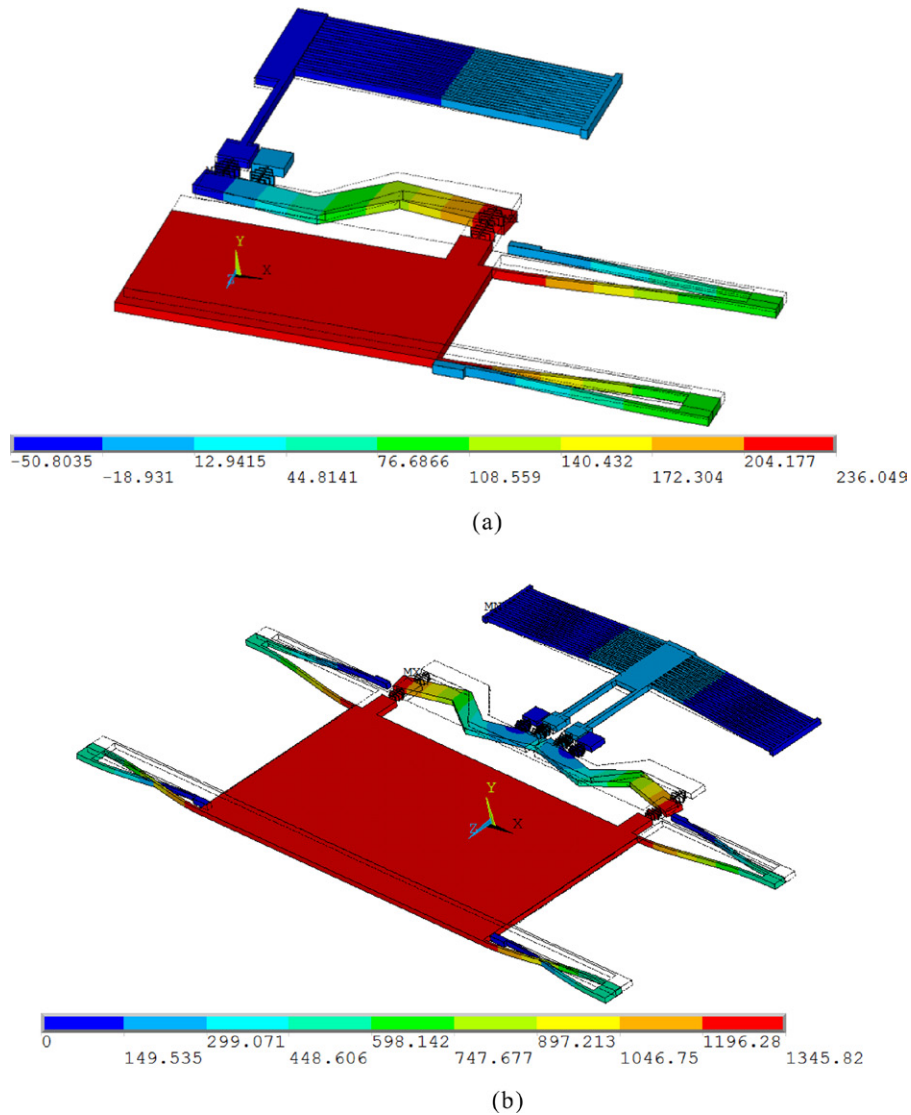


Figure 9. Finite element analysis (FEA) results. (a) The expected deformation of the folded spring with the beam flexure. (b) The expected response at the first resonant frequency.

linked to a connecting block made of the handle layer of the SOI wafer.

5. Experimental results

5.1. The range of motion of the MEMS motion stage

The motion stages with the three different types of flexures were fabricated and tested to measure their maximum motion displacement at first. For this experiment, two metal pads near the actuator are electrically connected to a direct current (DC) power supply and the corresponding motion is measured by an optical profiler, VEECO NT1100⁴ [41]. The motion stages displacement results are summarized and plotted in figure 11. The maximum displacement of the motion stage is measured to be 80 μm with the beam flexure, 76 μm with the cartwheel flexure, and 28 μm with the butterfly flexure, respectively. The motion stage with the cartwheel flexure shows a performance similar to the beam flexure, because the rotational stiffness of the cartwheel is similar to that of the beam flexure. However, a

decrease in performance is observed for a displacement larger than 70 μm , which comes from the geometric discrepancy in the lever mechanism and detailed in the following discussion section. The output of the moving stage using the butterfly flexure is relatively smaller than the others indicating that this flexure is not appropriate to convert the linear motion from the actuator into a rotational motion for the lever.

5.2. Out-of-plane deformation of the moving stage

The out-of-plane deformation of the fabricated motion stage under load is experimentally measured by placing a dead weight silicon block on the moving stage. The block applies a force of 120 μN to the moving stage. The 3D scanned images near the lever are shown in figure 12. The beam flexure and cartwheel flexure show the flagging of the moving stage less than 2 μm .

The displacements of the moving stage from its supporting frame with this additional weight are measured and plotted in figure 13. The motion stage with the beam flexure is more

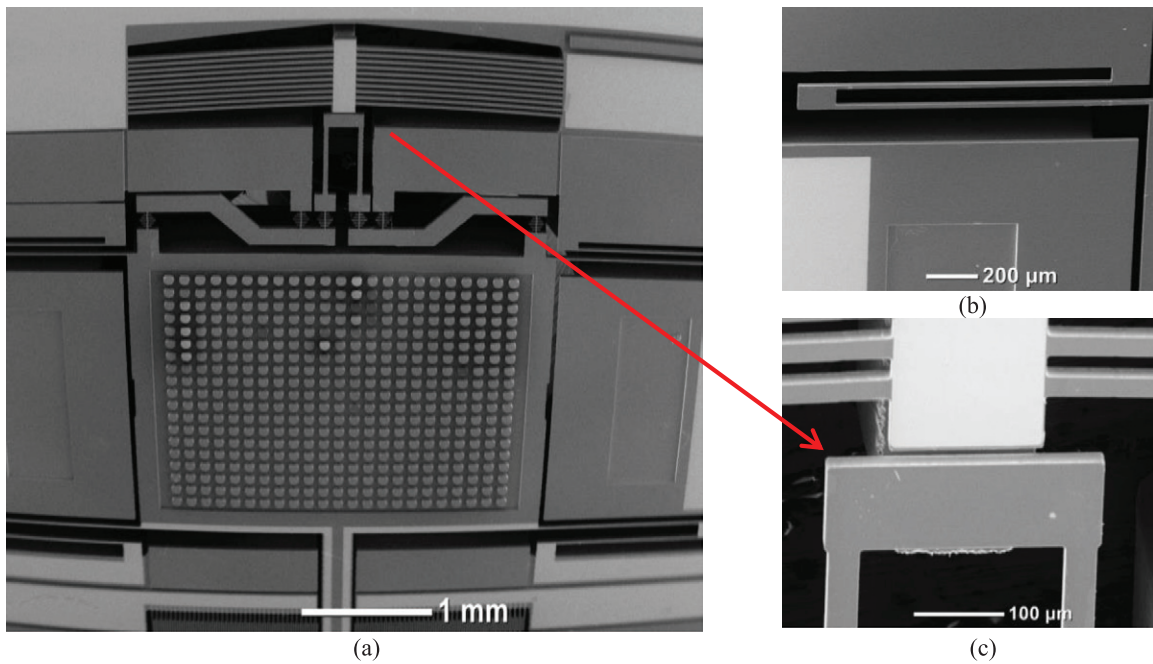


Figure 10. Scanning electron microscope (SEM) images of the MEMS-based motion stage. (a) SEM image of the fabricated motion stage. (b) The folded spring. (c) Close up view near the actuator.

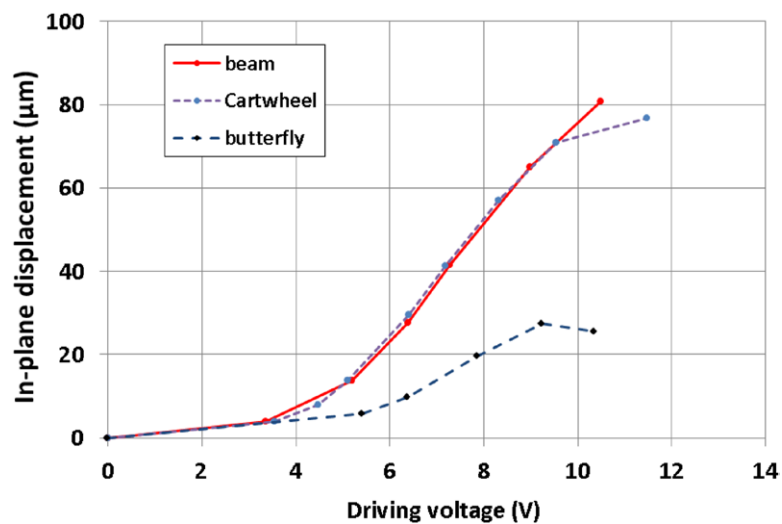


Figure 11. The experimentally measured displacement of the motion stages with three types of flexures.

flexible than the others along an out-of-plane direction, as shown in figure 13(a). The stiffness of the cartwheel is greater than the other designs and the levers are attached to only one side of the moving stage, so the moving stage tends to tilt as shown in figure 13(b). The out-of-plane deformation with the butterfly flexure is measured around $1.2 \mu\text{m}$ for 1.2 mm length. This is shown in figure 13(c) and is positioned between the other two flexures.

The out-of-plane deformation is also measured while the motion stage is in operation. This is measured at the moving stage close to the levers and is plotted in figure 14. The motion stage with the beam flexure shows an additional out-of-plane deformation of $1.5 \mu\text{m}$ when it generates a motion greater than $65 \mu\text{m}$. The motion stage with the cartwheel flexure tends to have a smaller out-of-plane deformation than the one with the

beam flexures. However, the motion stage with the cartwheel flexures tends to fail near $75 \mu\text{m}$ displacement, which is earlier than the one with the beam flexures. It is difficult to maintain the motion stage stiffness because of the out-of-plane deformation with the butterfly flexure. Based on these observations, without the additional weight the cartwheel flexure is expected to show a larger stiffness against out-of-plane deformation than the others.

6. Discussion

In this section, the finite element (FE) models of the three joints are built to analyze their performance. Based on the measured dimensions of the three types of flexures, their corresponding 3D models are constructed in SolidWorks⁴

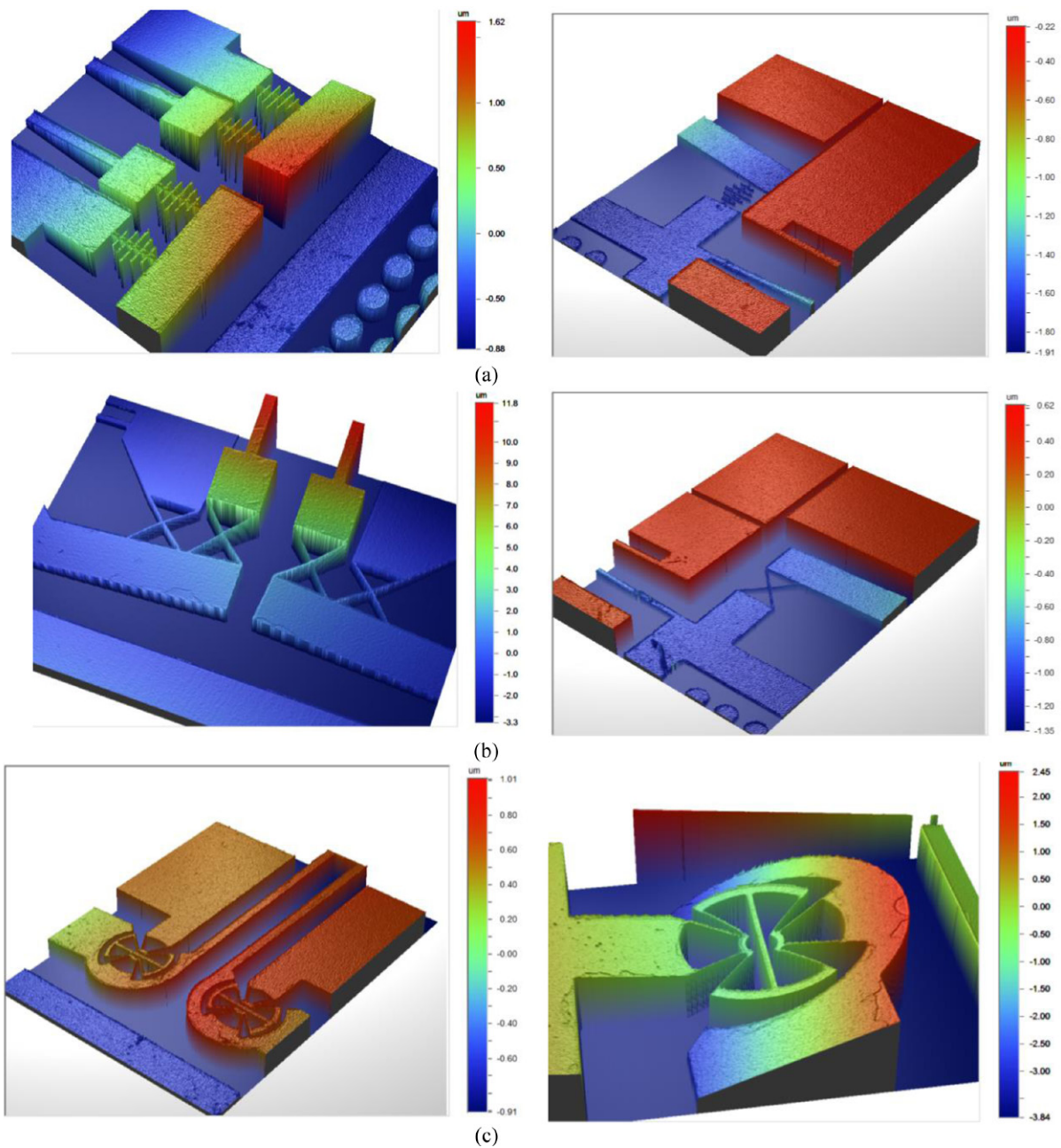


Figure 12. The scanned 3D images of the three types of flexures (unit in μm). (a) The beam flexure. (b) The cartwheel flexure. (c) The butterfly flexure.

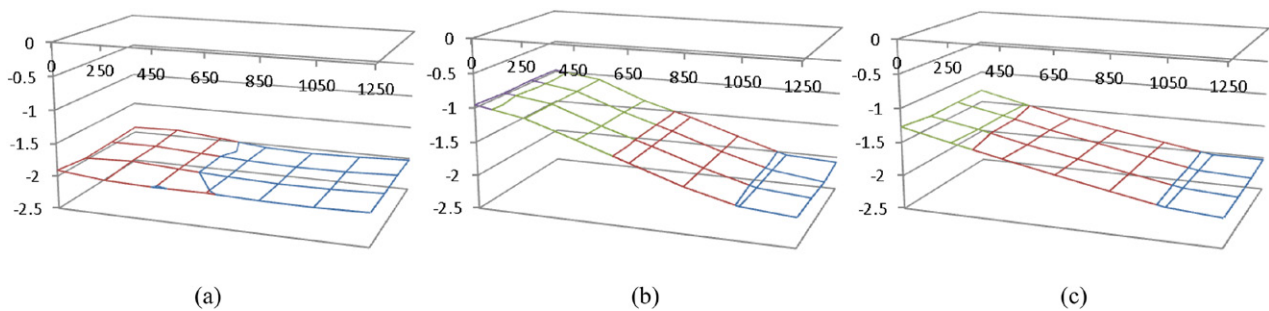


Figure 13. The dragging of the moving stage by three types of flexures for an external force of $32 \mu\text{N}$ on the stage (unit in μm). (a) The beam flexure. (b) The cartwheel flexure. (c) The butterfly flexure.

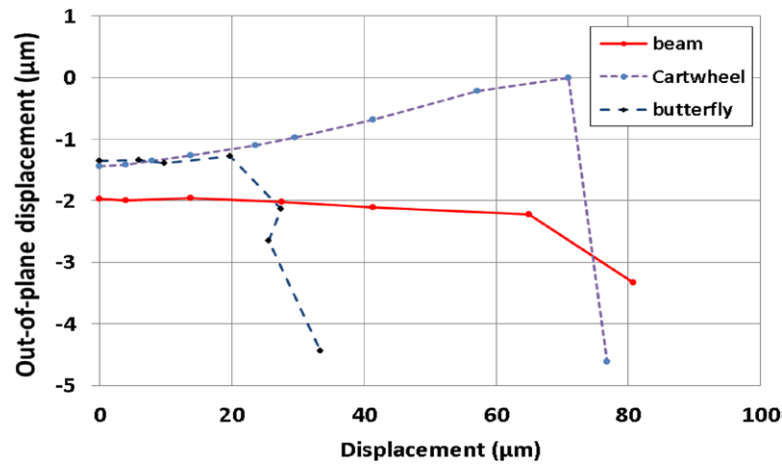


Figure 14. The change of the out-of-plane deformation in the presence of an external force of $32 \mu\text{N}$ on the stage.

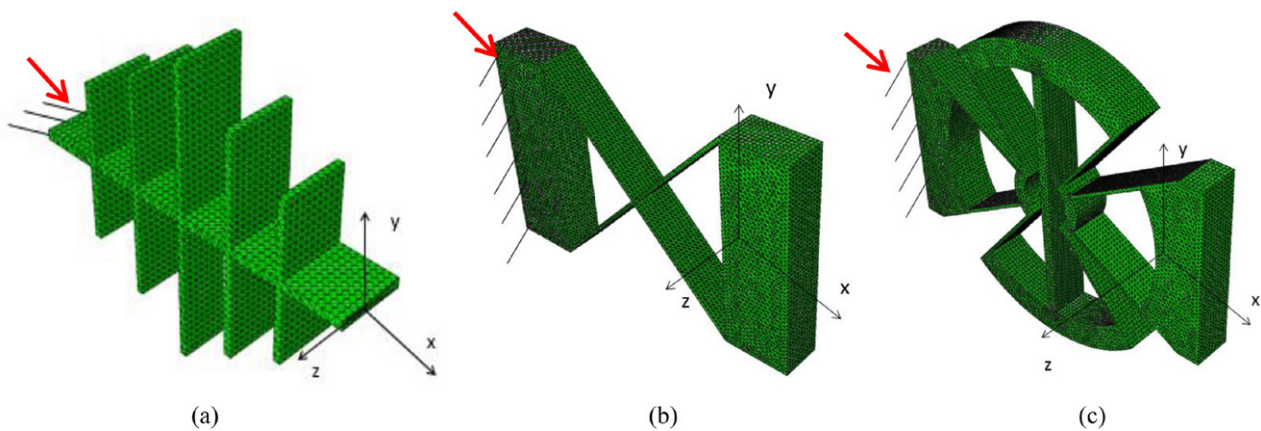


Figure 15. Finite element modeling of the three hinge joints. (a) The beam flexure. (b) The cartwheel flexure. (c) The butterfly flexure.

Table 2. The rotational displacement of the three types of flexures when the moments are applied to the flexures.

Flexure type	Moment	Θ_x (radian)	Θ_y (radian)	Θ_z (radian)
Beam	M_x ($10 \text{ mN}\cdot\mu\text{m}$)	3.56×10^{-2}	-2.27×10^{-7}	-2.25×10^{-5}
	M_y ($10 \text{ mN}\cdot\mu\text{m}$)	-5.62×10^{-7}	1.31×10^{-3}	-1.99×10^{-6}
	M_z ($1 \text{ mN}\cdot\mu\text{m}$)	4.41×10^{-7}	-7.16×10^{-8}	6.94×10^{-3}
Cartwheel	M_x ($10 \text{ mN}\cdot\mu\text{m}$)	7.31×10^{-4}	-2.70×10^{-5}	-3.10×10^{-6}
	M_y ($10 \text{ mN}\cdot\mu\text{m}$)	-2.7×10^{-5}	2.59×10^{-3}	-2.87×10^{-6}
	M_z ($1 \text{ mN}\cdot\mu\text{m}$)	-1.74×10^{-9}	-8.92×10^{-8}	3.28×10^{-3}
Butterfly	M_x ($10 \text{ mN}\cdot\mu\text{m}$)	6.53×10^{-3}	-1.49×10^{-7}	-1.98×10^{-6}
	M_y ($10 \text{ mN}\cdot\mu\text{m}$)	4.77×10^{-7}	6.34×10^{-3}	-3.89×10^{-7}
	M_z ($1 \text{ mN}\cdot\mu\text{m}$)	-8.51×10^{-8}	-1.92×10^{-8}	2.78×10^{-3}

based on the analysis used for multi degrees of freedom (DOF) model [42, 43]. For simulation, one end of each flexure is fixed as indicated by the red arrows in figure 15 and the other end is utilized for the corresponding coordinate system as shown in figure 15. A kinematic constraint of six degrees of freedom (DOF) is built on the plane where the coordinate is located [44, 45]. This plane is defined as the slave plane while the origin of the coordinate system is defined as the control point. For the beam flexure and cartwheel flexure, the slave planes are consistent rectangular planes. The slave plane of the butterfly flexure is the curved plane. At the origin of the

coordinate, the moments along the three axes are applied. By means of this setting, the plane of the free end moves as a whole rigid plane when the loading is located at the origin of the coordinate. As shown in figure 15, the FE models of the three joints are meshed with 21 835, 124 207, and 155 336 tetrahedral elements, respectively. Table 2 presents the moment applied on the origins. The subscripts denote the directions of the moments along the axes of the coordinates in figure 15, respectively.

Based on the moment applied to the flexures, the corresponding rotational angles along the three directions are also

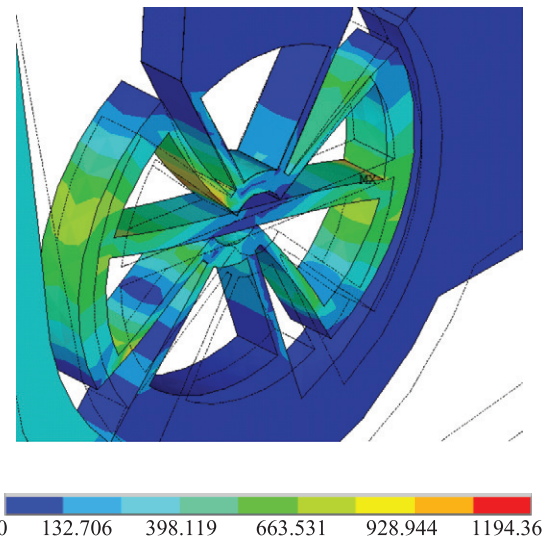
Table 3. The translational displacement of the three types of flexures when the forces are applied to the origin of the coordinate shown in figure 15.

Flexure type	Force	Δx (μm)	Δy (μm)	Δz (μm)
Beam	F_x (10 mN)	9.80×10^{-2}	-1.01×10^{-4}	-9.25×10^{-5}
	F_y (10 μN)	-1.25×10^{-3}	5.72×10^{-1}	-1.61×10^{-6}
	F_z (100 μN)	-4.66×10^{-5}	-4.56×10^{-4}	1.10×10^{-1}
Cartwheel	F_x (10 mN)	1.99×10^{-1}	5.27×10^{-3}	-2.63×10^{-4}
	F_y (10 μN)	-2.58×10^{-4}	1.87×10^{-1}	5.11×10^{-6}
	F_z (100 μN)	-1.62×10^{-4}	-9.77×10^{-5}	2.02×10^{-1}
Butterfly	F_x (10 mN)	1.78×10^{00}	1.60×10^{-4}	2.15×10^{-4}
	F_y (10 μN)	-4.07×10^{-4}	3.10×10^{-1}	-4.89×10^{-7}
	F_z (100 μN)	-2.01×10^{-3}	-3.58×10^{-5}	7.83×10^{-1}

summarized and listed in table 2. The moment M_z is related to the in-plane stiffness of the presented motion stage and table 2 shows that the beam flexure is more flexible than the others. This indicates that the in-plane motion with the beam flexure will be larger than the others. Contrary to this, the butterfly flexure is expected to generate an in-plane displacement smaller than the others, because of its complex structure. The analysis described here matches with the experiments shown in figures 11 and 12. It explains the differences among three flexures.

The unwanted out-of-plane deformation is another factor that is analyzed using FEA, because when a sample is placed on the moving stage, its weight can cause an out-of-plane deformation and thus result in errors in the experiments. These FEA results explain well the experimental results of section 5.2 about the out-of-plane deformation. Since the flexure is also related to the lever mechanism, the motion θ_x is more dominant than θ_y . This is because the dimension of the lever along the y direction is much larger than the x direction indicating that a larger moment is expected along the x direction. The column of θ_x in table 2 shows that the beam type is more flexible than the other types for the out-of-plane deformations and the cartwheel flexure is stiffer than the others. This comparison implies that the out-of-plane deformation can be minimized with the cartwheel flexure. Based on these comparisons, the beam flexure is preferred for a larger displacement and the cartwheel flexure is preferred for reducing out-of-plane deformation.

Table 3 shows the list of the deformation results when a force is applied to the origin of the coordinate shown in figure 15. This translational deformation is important to evaluate the performance of the pivoted hinge or flexure. To achieve reasonable operation of a lever, the pivot should be flexible for the rotational motion along the Z -axis, but be firm against any other rotational or translational motions. The one end of the lever is linked to the actuator to generate a pure linear motion, not a rotary motion. This indicates that the pivot in the lever experiences both rotational motion and translational motion. In order to check this, the responses of the flexures are calculated by the X , Y , and Z translational forces, respectively. In table 3, the butterfly flexure is more flexible than the others and the beam flexure is the stiffest

**Figure 16.** The expected mechanical deformation of the pivoted butterfly flexure (unit in μm).

among them. In this case, the butterfly flexure is hard to operate as a pivot efficiently, because some portion of the force will be used to compress the butterfly flexure itself, and not generate a rotational motion. Contrary to this, the beam flexure is expected to operate as a pivot efficiently. Figure 16 shows the expected mechanical deformation of the butterfly flexure, which tends to be squeezed when the translational displacement of the actuator is applied to the joint.

Another feature to check is the stiffness against the transverse force or the response for the force F_y . The two levers are connected to the moving stage in a symmetric layout. In this case, when the lever rotates, the flexures at the ends of the lever will experience shear deformation indicated by Δy in figure 17, which will result in a Δy displacement deformation. In order to reduce the effect from this additional deformation, it is desirable to maintain a low stiffness along the Y axis. In table 3, the beam flexure is more flexible than the other designs along this direction and the cartwheel flexure is the stiffest among them. This difference can cause a noticeable performance difference at a large displacement as shown in figure 11.

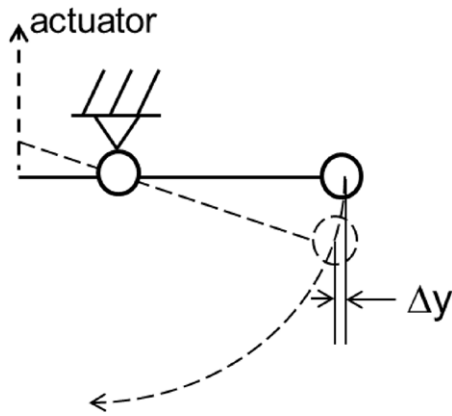


Figure 17. The expected deformation of the lever in operation.

7. Conclusions

The design, analysis, fabrication, and testing of a MEMS-based 1-DOF motion stage are presented for practical applications with a large displacement and sufficient force. The specification for a rheological application is utilized as a reference in the design process. For these design goals, the presented motion stage utilizes several features: (1) the optimized bent-beam type thermal actuator for providing adequate force; (2) the well-balanced levers with three different types of flexures for a large displacement; and (3) a moving stage of $3.2\text{ mm} \times 2.7\text{ mm}$ as a test bed supported by four folded springs.

Through these design processes, the presented motion stage is able to generate up to $80\ \mu\text{m}$ displacement with the beam flexure and less than $1\ \mu\text{m}$ out-of-plane deformation with the cartwheel flexure. Compared with previous designs, the expected shear pressure ranges from $794\ \text{Pa}$ to $7.93\ \text{kPa}$, which are within the range of conventional rheometers.

For reliable operation, the presented design is fabricated with three types of flexures and their in-plane displacement and out-of-plane deformation are measured experimentally. Based on these experiments and FEA results, the beam flexure is regarded as a desirable flexure for a large displacement, but weak for out-of-plane deformation. The cartwheel shows a good performance in reducing the out-of-plane deformation but its in-plane stiffness is relatively larger than the beam flexure, which is a not good for a large displacement. The geometric issue of the lever is also mentioned in the discussion session where the additional stiffness for a displacement larger than $70\ \mu\text{m}$ can cause poor performance with the cartwheel flexure. The butterfly flexure is designed for a pure rotational motion, so it is inappropriate for the use of this lever which has to convert a translational motion into a rotation motion.

The presented MEMS-based motion stage is designed based on practical requirements, so this stage can be utilized in various metrological applications, especially a rheological measurement utilizing its large moving stage or micro-manipulations applications by placing an object on its moving stage without significant deformations. In addition, the analysis and the testing of the three types of flexures can be a guide in the design and application of various flexural mechanisms, such as amplifying mechanisms, positioning stage, and sensors among others.

Acknowledgments

This research was performed in part at the NIST Center for Nanoscale Science and Technology (CNST) Nano Fabrication Clean Room. This work was partially supported by the Sustainable Engineered Materials Program of the Materials and Structural Systems Division, Engineering Laboratory, National Institute of Standards and Technology, USA.

References

- [1] Choi Y-M, Gorman J J, Dagalakis N G, Yang S H, Kim Y S and Yoo J M 2012 A high-bandwidth electromagnetic MEMS motion stage for scanning applications *J. Micromech. Microeng.* **22** 105012
- [2] Chowdhury S, Svec P, Wang C, Seale K T, Wikswow J P, Losert W and Gupta S K 2013 Automated cell transport in optical tweezers-assisted microfluidic chambers *IEEE Trans. Autom. Sci. Eng.* **10** 980–9
- [3] Chowdhury S, Thakur A, Svec P, Wang C, Losert W and Gupta S K 2014 Automated manipulation of biological cells using gripper formations controlled by optical tweezers *IEEE Trans. Autom. Sci. Eng.* **11** 338–47
- [4] Shi H, Duan X and Su H-J 2014 Optimization of the workspace of a MEMS hexapod nanopositioner using an adaptive genetic algorithm *IEEE Int. Conf. on Robotics and Automation (Hong Kong)* pp 4043–8
- [5] Fan L, Wu M C, Choquette K D and Crawford M H 1997 Self-assembled microactuated XYZ stages for optical scanning and alignment *Int. Conf. on Solid State Sensors and Actuators TRANSDUCERS'97 (Chicago)* (IEEE) vol 1 pp 319–22
- [6] Cao A, Kim J and Lin L 2007 Bi-directional electrothermal electromagnetic actuators *J. Micromech. Microeng.* **17** 975
- [7] Kim Y-S, Yoo J-M, Yang S H, Choi Y M, Dagalaks N G and Gupta S K 2012 Design, fabrication and testing of a serial kinematic MEMS XY stage for multifinger manipulation *J. Micromech. Microeng.* **22** 085029
- [8] Yang S H, Kim Y-S, Yoo J-M and Dagalakis N G 2012 Microelectromechanical systems based Stewart platform with sub-nano resolution *Appl. Phys. Lett.* **101** 061909
- [9] Kim C-H and Kim Y-K 2002 Micro XY-stage using silicon on a glass substrate *J. Micromech. Microeng.* **12** 103
- [10] Oliver A D, Vigil S R and Gianchandani Y B 2003 Photothermal surface-micromachined actuators *IEEE Trans. Electron Devices* **50** 1156–7
- [11] Chu L L and Gianchandani Y B 2003 A micromachined 2D positioner with electrothermal actuation and sub-nanometer capacitive sensing *J. Micromech. Microeng.* **13** 279
- [12] P-611.3 NanoCube[®] XYZ piezo stage compact multi-axis piezo system for nanopositioning and fiber alignment (www.physikinstrumente.com/product-detail-page/p-6113-201700.html)
- [13] Christopher G F, Yoo J M, Dagalakis N, Hudson S D and Migler K B 2010 Development of a MEMS based dynamic rheometer *Lab Chip* **10** 2749–57
- [14] Ferraris C F, Li Z, Zhang M-H and Stutzman P 2013 Development of a reference material for the calibration of cement paste rheometers *Adv. Civ. Eng. Mat.* **2** 140–62
- [15] Chan R W and Rodriguez M L 2008 A simple-shear rheometer for linear viscoelastic characterization of vocal fold tissues at phonatory frequencies *J. Acoust. Soc. Am.* **124** 1207–19
- [16] Struble L J and Schultz M A 1993 Using creep and recovery to study flow behavior of fresh cement paste *Cement Concr. Res.* **23** 1369–79

- [17] Sun Z, Voigt T and Shah S P 2006 Rheometric and ultrasonic investigations of viscoelastic properties of fresh Portland cement pastes *Cement Concr. Res.* **36** 278–87
- [18] Marin G, Collyer A A and Clegg D W 1988 *Rheological Measurements* ed A A Collyer and D W Clegg (Netherlands: Springer) (doi:10.1007/978-94-011-4934-1)
- [19] Johnstone R W and Parameswaran M 2001 Self-assembly of surface-micromachined structures using electrostatic attraction *Proc. SPIE* **4561** 66–76
- [20] Olfatnia M, Sood S, Gorman J J and Awtar S 2013 Large stroke electrostatic comb-drive actuators enabled by a novel flexure mechanism *J. Microelectromech. Syst.* **22** 483–94
- [21] Chiou J-C, Lin Y-J and Kuo C-F 2008 Extending the traveling range with a cascade electrostatic comb-drive actuator *J. Micromech. Microeng.* **18** 015018
- [22] Kim K H, Yoon H J, Jeong O C and Yang S S 2005 Fabrication and test of a micro electromagnetic actuator *Sensors Actuators* **117** 8–16
- [23] Lee C-Y, Chang H-T and Wen C-Y 2008 A MEMS-based valveless impedance pump utilizing electromagnetic actuation *J. Micromech. Microeng.* **18** 035044
- [24] Baker M S, Walraven J A, Headley T J and Plass R A 2004 *Final Report: Compliant Thermo-mechanical MEMS Actuators*, LDRD# 52553 (Albuquerque, NM: United States Department of Energy)
- [25] Chen W-C, Yeh P-I, Hu C-F and Fang W 2008 Design and characterization of single-layer step-bridge structure for out-of-plane thermal actuator *J. Microelectromech. Syst.* **17** 70–7
- [26] Park J-S, Chu L L, Siwapornsathain E, Oliver A D and Gianchandani Y B 2000 Long throw and rotary output electro-thermal actuators based on bent-beam suspensions *The 13th Annual Int. Conf. on Micro Electro Mechanical Systems* pp 680–5
- [27] Bergna S, Gorman J J and Dagalakis N G 2005 Design and modeling of thermally actuated MEMS nanositioners *ASME 2005 Int. Mechanical Engineering Congress and Exposition* pp 561–8
- [28] Franz L and Andrea S 1996 Method of anisotropically etching silicon *US Patent Specification* 5501893
- [29] Brouwer D M, De Jong B R and Soemers H 2010 Design and modeling of a six DOFs MEMS-based precision manipulator *Precis. Eng.* **34** 307–19
- [30] Que L, Park J-S and Gianchandani Y B 2001 Bent-beam electrothermal actuators-part I: single beam and cascaded devices *J. Microelectromech. Syst.* **10** 247–54
- [31] Zhu Y, Corigliano A and Espinosa H D 2006 A thermal actuator for nanoscale *in situ* microscopy testing: design and characterization *J. Micromech. Microeng.* **16** 242
- [32] Jones R M 2006 *Buckling of Bars, Plates, and Shells* (Blacksburg, VA: Bull Ridge Corporation)
- [33] Komkov V, Choi K K and Haug E J 1986 *Design Sensitivity Analysis of Structural Systems* (New York: Academic)
- [34] Fong N J T, deWit R, Marcal P V, Filliben J J and Heckert N A 2009 *A Design-of-Experiments Plug-In for Estimating Uncertainties in Finite Element Simulations, Presented at the SIMULIA Customer Conf. (London)* pp 828–42
- [35] Heckert N A An EDA approach to experimental design (<http://itl.nist.gov/div898/handbook/pri/section5/pri59.htm>)
- [36] Montgomery D C 2012 *Design and Analysis of Experiments* 8th edn (Hoboken, NJ: Wiley)
- [37] Kang D and Gweon D 2012 Development of flexure based 6-degrees of freedom parallel nano-positioning system with large displacement *Rev. Sci. Instrum.* **83** 035003
- [38] Stranczl M, Sarajlic E, Fujita H, Gijs M A M and Yamahata C 2012 High-angular-range electrostatic rotary stepper micromotors fabricated with SOI technology *J. Microelectromech. Syst.* **21** 605–20
- [39] Petersen K E 1982 Silicon as a mechanical material *Proc. IEEE* **70** 420–57
- [40] Cowen A, Hames G, Monk D, Wilcenski S and Hardy B 2011 *SOIMUMPs Design Handbook* (MEMScAP Inc) pp 2002–11
- [41] DMEMS Dynamic MEMS Measurement Option for Wyko NT1100 Optical Profilers (www.veeco.com/company/news/veeco-introduces-nt-9100-s-optical-profiling-system)
- [42] Shi H, Su H-J and Dagalakis N 2014 A stiffness model for control and analysis of a MEMS hexapod nanositioner *Mech. Mach. Theory* **80** 246–64
- [43] Shi H and Su H-J 2013 An analytical model for calculating the workspace of a flexure hexapod nanositioner *ASME J Mech. Robot.* **5** 041009
- [44] Shi H 2013 Modeling and analysis of compliant mechanisms for designing nanositioners *PhD Dissertation* The Ohio State University, Columbus, OH, USA
- [45] Shi H and Su H-J 2012 Workspace of a flexure hexapod nanositioner *Proc. of ASME IDETC/CIE (Chicago, Illinois, 12–15 August 2012)*